

# ExoMol line lists – LXIII: ExoMol line lists for 12 isotopologues of CO<sub>2</sub>

Sergei N. Yurchenko<sup>\*</sup>, Marco G. Barnfield, Charles A. Bowesman, Ryan P. Brady,  
Elizabeth R. Guest, Kyriaki Kefala, Qing-He Ni, Armando N. Perri, Oleksiy A. Smola,  
Andrei Solokov, Chenyi Tao, Jonathan Tennyson<sup>†</sup>,  
*Department of Physics and Astronomy, University College London, Gower Street, WC1E 6BT London, United Kingdom*

Accepted XXXX. Received XXXX; in original form XXXX

## ABSTRACT

Extensive rovibrational line lists are constructed for 12 isotopologues of carbon dioxide: <sup>12</sup>C<sup>16</sup>O<sub>2</sub>, <sup>13</sup>C<sup>16</sup>O<sub>2</sub>, <sup>12</sup>C<sup>17</sup>O<sub>2</sub>, <sup>13</sup>C<sup>17</sup>O<sub>2</sub>, <sup>12</sup>C<sup>18</sup>O<sub>2</sub>, <sup>13</sup>C<sup>18</sup>O<sub>2</sub>, <sup>16</sup>O<sup>12</sup>C<sup>17</sup>O, <sup>16</sup>O<sup>12</sup>C<sup>18</sup>O, <sup>16</sup>O<sup>13</sup>C<sup>17</sup>O, <sup>16</sup>O<sup>13</sup>C<sup>18</sup>O, <sup>17</sup>O<sup>12</sup>C<sup>18</sup>O, and <sup>17</sup>O<sup>13</sup>C<sup>18</sup>O. The variational program TROVE was employed together with an exact kinetic energy operator, accurate empirical potential energy surface (Ames-2) and the *ab initio* dipole moment surface Ames-2021-40K. Empirical energy levels from the most recent MARVEL analyses, as well as from the HITRAN and CDSD databases, are used to replace calculated values where available. The line lists are further supplemented by assigning AFGL quantum numbers using machine-learning based estimators. The resulting data were employed to generate opacities with four radiative transfer codes, TauREx, ARCIS, NEMESIS, and petitRADTRANS, both for individual isotopologues and for CO<sub>2</sub> at terrestrial isotopic natural abundance. All line lists and associated data are available at [www.exomol.com](http://www.exomol.com).

**Key words:** molecular data - opacity - planets and satellites: atmospheres - stars: atmospheres - ISM: molecules.

<sup>\*</sup> The corresponding author: [s.yurchenko@ucl.ac.uk](mailto:s.yurchenko@ucl.ac.uk)

<sup>†</sup> The corresponding author: [j.tennyson@ucl.ac.uk](mailto:j.tennyson@ucl.ac.uk)

## 1 INTRODUCTION

Carbon dioxide ( $\text{CO}_2$ ) is a key atmospheric constituent across a wide range of planetary environments, including Earth (Oyafuso et al. 2017), Venus (Fedorova et al. 2015; Snels et al. 2014), and Mars (Refaat & Singh 2024; Webster et al. 2013), as well as exoplanets (Oppenheimer et al. 2013; Swain et al. 2009b,a; Heng & Lyons 2016) and brown dwarfs (Freedman et al. 2014; Line et al. 2017). In the Earth’s atmosphere,  $\text{CO}_2$  is the second most abundant greenhouse gas after water vapour (Oyafuso et al. 2017), and is therefore central to studies in environmental chemistry. Several dedicated missions (Butz et al. 2011; Crisp et al. 2004; Abshire et al. 2010) monitor Earth’s atmospheric  $\text{CO}_2$  content. Since  $\text{CO}_2$  is a major component of the atmospheres of Earth, Mars, and Venus, remote sensing of this molecule is expected to be equally important for characterising exoplanets with similar properties. For example,  $\text{CO}_2$  dominates the opacity of the Venusian atmosphere, comprising approximately 95% of its composition (Pollack et al. 1993). The critical role of  $\text{CO}_2$  in atmospheric retrievals has been highlighted in multiple planetary science studies ranging from terrestrial remote sensing (e.g. Roche et al. (2021)) to planetary atmospheres such as Mars (e.g., Jiménez-Monferrer et al. (2021)).

In the context of exoplanetary science,  $\text{CO}_2$  is anticipated to be a key molecular absorber across a broad range of planetary types, from temperate terrestrial planets to hot Jupiters. Its strong  $4.3\ \mu\text{m}$  band has been unambiguously detected with JWST in the atmospheres of WASP-39 b (Ahrer et al. 2023), WASP-166 b (Mayo et al. 2025), and the sub-Neptune K2-18 b (Madhusudhan et al. 2023; Holmberg & Madhusudhan 2024). Consequently, comprehensive and accurate opacity data for  $\text{CO}_2$  and its isotopologues, valid over wide spectral and temperature ranges, are essential for probing atmospheric composition and physical conditions such as temperature and pressure. Such data underpin high-accuracy atmospheric models and are crucial for interpreting spectroscopic observations from ground-based telescopes and space missions, including JWST and the future ESA space observatory Ariel (Chubb et al. 2024).

Detection of  $\text{CO}_2$  with high-resolution spectroscopy has not yet been achieved, mainly due to challenges associated with telluric contamination (Carleo et al. 2022), although searches are ongoing (Biassoni et al. 2024). Isotopic ratios, in particular  $^{13}\text{C}^{16}\text{O}_2/^{12}\text{C}^{16}\text{O}_2$ , have been proposed as tracers of carbon isotope fractionation in exoplanetary atmospheres, with potential links to biological processes detectable by JWST (Glidden et al. 2023). Recently, four isotopologues of  $\text{CO}_2$  –  $^{12}\text{C}^{16}\text{O}_2$ ,  $^{13}\text{C}^{16}\text{O}_2$ ,  $^{16}\text{O}^{12}\text{C}^{18}\text{O}$ , and  $^{16}\text{O}^{12}\text{C}^{17}\text{O}$  – were detected in a terrestrial planet-forming region of an externally irradiated Herbig disk using VLT (Frediani et al. 2025).

Significant progress in developing high-resolution, variationally computed  $\text{CO}_2$  line lists has been made in recent years by the NASA Ames group (Huang et al. 2012, 2014, 2017, 2013) and the ExoMol project (Zak et al. 2016, 2017a,b; Yurchenko et al. 2020). High-temperature line lists are particularly important for modelling exoplanetary atmospheres, and numerous works have targeted this goal (Huang et al. 2014, 2017; Wattson & Rothman 1986; Tashkun et al. 2003; Tashkun & Perevalov 2011; Rothman et al. 2010; Huang et al. 2013; Yurchenko et al. 2020). Recent high-temperature datasets include UCL-4000 (Yurchenko et al. 2020), Ames-2021 (Huang et al. 2022), the latest Ames line lists AI-3000K (Huang et al. 2023) and its HITEMP compilation (Hargreaves et al. 2024). An accurate room-temperature line list CDSD-2024-PI was recently reported by Kochanov & Perevalov (2025). While ExoMol and Ames line lists combine experimental results with variational calculations, improved with empirically-derived energies, the CDSD-2024-PI (Tashkun et al. 2015) and HITRAN (Gordon et al. 2022; Karlovets et al. 2021) line lists rely on effective Hamiltonian models. All provide accurate and comprehensive rovibrational data for  $\text{CO}_2$ , but further improvements in accuracy and completeness remain necessary.

An additional aspect relevant to this work is the treatment of pressure broadening. A large body of literature exists on  $\text{CO}_2$  broadening coefficients with different perturbing species; here we only highlight a few recent developments. Gamache & Lamouroux (2013) presented a detailed analysis of a large set of experimental broadening parameters for the main isotopologue colliding with  $\text{N}_2$ ,  $\text{O}_2$ , and  $\text{CO}_2$ , with further analyses and reassessments reported by Gamache et al. (2014) and Hashemi et al. (2020).

In this work we present extensive rovibrational line lists for 12 isotopologues of  $\text{CO}_2$ :  $^{12}\text{C}^{16}\text{O}_2$ ,  $^{13}\text{C}^{16}\text{O}_2$ ,  $^{12}\text{C}^{17}\text{O}_2$ ,  $^{13}\text{C}^{17}\text{O}_2$ ,  $^{12}\text{C}^{18}\text{O}_2$ ,  $^{13}\text{C}^{18}\text{O}_2$ ,  $^{16}\text{O}^{12}\text{C}^{17}\text{O}$ ,  $^{16}\text{O}^{12}\text{C}^{18}\text{O}$ ,  $^{16}\text{O}^{13}\text{C}^{17}\text{O}$ ,  $^{16}\text{O}^{13}\text{C}^{18}\text{O}$ ,  $^{17}\text{O}^{12}\text{C}^{18}\text{O}$ , and  $^{17}\text{O}^{13}\text{C}^{18}\text{O}$ . The line lists were generated with TROVE (Yurchenko et al. 2007) using an exact kinetic energy operator (KEO), the empirical potential energy surface (PES) Ames-2 (Huang et al. 2017) and the *ab initio* dipole moment surface (DMS) Ames-2021-40K (Huang et al. 2023). To improve line position accuracy, (i) we employed the empirical band-centre correction approach (Yurchenko et al. 2011; Mant et al. 2018), shifting the diagonal vibrational Hamiltonian terms to match experimental values, followed by (ii) substitution of calculated energy levels with empirical ones from MARVEL studies (Ibrahim et al. 2024; Alatoom et al. 2024; Azzam et al. 2024, 2025a,b; Obaidata et al. 2025; Mansour et al. 2025; Azzam et al. 2025c), HITRAN (Gordon et al. 2022; Karlovets et al. 2021), and CDSD-2024-PI (Kochanov & Perevalov 2025). As part of this work, empirical energies of the minor  $\text{CO}_2$  isotopologues were extracted from HITRAN using the MARVEL procedure.

The resulting line lists, in ExoMol format (Tennyson et al. 2013, 2024b), contain energies, Einstein A coefficients, lifetimes, uncertainties, and quantum numbers for 12 isotopologues of  $\text{CO}_2$ . Partition functions and broadening parameters are also provided. Associated opacities were computed for the four radiative transfer codes ARCiS (Min et al. 2020), TauREx (Al-Refaie et al. 2021), NEMESIS (Irwin et al. 2008) and petitRADTRANS (Mollière et al. 2019) using the ExoMolOP procedure (Chubb

et al. 2021), both for individual isotopologues and for a composite opacity assuming terrestrial isotopic abundances. All data are available from the ExoMol database at [www.exomol.com](http://www.exomol.com).

## 2 ROVIBRATIONAL STATES OF CO<sub>2</sub> ISOTOPOLOGUES: QUANTUM NUMBERS AND SELECTION RULES

Accurate description of the rovibrational states is essential for the construction and assignment of spectroscopic line lists. Quantum numbers provide the link between the variationally computed eigenstates of CO<sub>2</sub> and the spectroscopic notation used in experimental and atmospheric studies. For CO<sub>2</sub> and its isotopologues, several labelling schemes exist, reflecting both the linear triatomic structure of the molecule and the strong Fermi-resonance interactions that complicate vibrational assignments. In addition, nuclear-spin statistics and molecular symmetry play a central role in determining the allowed rovibrational levels and transition selection rules. In the following subsections we outline the quantum number conventions, symmetry classifications, and selection rules adopted in this work, following both spectroscopic practice and the requirements of large-scale automatic assignments.

Vibrational states of symmetric (non-linear) XY<sub>2</sub> molecules can be described by three normal modes, conventionally denoted as  $\nu_1$  (symmetric stretch),  $\nu_2$  (bend), and  $\nu_3$  (asymmetric stretch). For linear symmetric triatomic molecules such as CO<sub>2</sub>, Herzberg’s notation is commonly used to label vibrational states. The three modes are associated with vibrational quantum numbers  $v_1$ ,  $v_2^{\ell_2}$ , and  $v_3$ . The superscript  $\ell_2$  denotes the vibrational angular momentum associated with the doubly-degenerate bending mode in the linear configuration. This quantum number represents the projection of the vibrational angular momentum along the molecular axis and takes values from  $-v_2$  to  $+v_2$  in steps of two. In spectroscopic notation, however, the absolute value  $|\ell_2|$  is often used.

The most widely adopted scheme for labelling vibrational states of CO<sub>2</sub> isotopologues is that of the Air Force Geophysics Laboratory (AFGL) (Amat & Pimbert 1965; Rothman & Young 1981; Toth et al. 2008). The AFGL notation employs a quintuplet of quantum numbers  $(m_1, m_2, l, m_3, r)$  designed to simplify the description of strong Fermi resonances in CO<sub>2</sub> of states  $\nu_1$  and  $2\nu_2$ , including their overtones and combination states, i.e. between states of the type  $(v_1, (v_2 + 2)^{\ell_2}, v_3)$  and  $(v_1 + 1, v_2^{\ell_2}, v_3)$ . The vibrational quantum numbers  $(m_1, m_2, m_3)$  are identical for all members of the same resonance polyad, while the fifth index  $r$  ranks the states within it. In AFGL notation,  $m_2$  and  $l$  are always equal, meaning  $l \geq l_2$ . By convention, for a given Fermi multiplet,  $r$  starts from 1 and increases by removing one quantum of  $\nu_1$  and adding two quanta of  $\nu_2$ . For example, the Fermi-resonant states  $(2, 0^0, 1)$ ,  $(1, 2^0, 1)$ , and  $(0, 4^0, 1)$  correspond to  $(20011)$ ,  $(20012)$ , and  $(20013)$ , respectively (Toth et al. 2008). The polyad number  $P = 2v_1 + v_2 + 3v_3$  is approximately conserved within a Fermi multiplet.

For asymmetric isotopologues such as <sup>16</sup>O<sup>12</sup>C<sup>17</sup>O, the AFGL quantum numbers follow the same scheme,  $(J, m_1, m_2, m_3, r, e/f)$ , even though the concepts of symmetric and asymmetric stretching lose their strict meaning. While AFGL notation provides a useful framework for analysing resonance clusters, it is not well suited for the automatic assignment of very large datasets.

### 2.1 Rotational quantum number and parity

The total angular momentum of CO<sub>2</sub> is denoted by  $J$ , which includes contributions from both overall molecular rotation and vibrational angular momentum ( $\ell_2 \neq 0$ ).

The Pauli principle imposes restrictions on symmetric isotopologues containing zero-spin oxygen nuclei, namely C<sup>16</sup>O<sub>2</sub> and C<sup>18</sup>O<sub>2</sub>. For these species, vibrational states with even  $v_3$  (symmetric under oxygen exchange) are only associated with even  $J$ , while states with odd  $v_3$  (antisymmetric) only allow odd  $J$ . This reflects the requirement that the total rovibrational wavefunction be symmetric under exchange of the two oxygen nuclei. The rotationless parity of a state is labelled  $e$  or  $f$  and is determined by the sum  $J + \ell_2 + v_3$ : states with even values correspond to  $e$  parity, and those with odd values to  $f$  parity.

For C<sup>17</sup>O<sub>2</sub> (<sup>12</sup>C<sup>17</sup>O<sub>2</sub> and <sup>13</sup>C<sup>18</sup>O<sub>2</sub>), the <sup>17</sup>O nuclei have non-zero spin ( $I = 5/2$ ). In this case the Pauli principle does not restrict odd or even levels, and both ortho and para nuclear-spin symmetries exist. All  $J$  values are allowed, and bands with  $\ell_2 > 0$  exhibit  $\ell$ -type doubling, giving rise to both  $e$  and  $f$  parity levels for each  $J$ .

### 2.2 Symmetry group classification

An alternative classification of rovibrational states uses molecular symmetry groups (Bunker & Jensen 1998), specifically C<sub>2v</sub>(M) or C<sub>s</sub>(M), and their irreducible representations (irreps). For symmetric CO<sub>2</sub>, states transform according to the C<sub>2v</sub>(M) group, which has four irreps:  $A_1$ ,  $A_2$ ,  $B_1$ , and  $B_2$ .

For isotopologues with zero-spin oxygen nuclei, the Pauli principle forbids rovibrational states of  $B_1$  and  $B_2$  symmetry,

**Table 1.** Nuclear spin statistical weights  $g_{\text{ns}}$  for CO<sub>2</sub> isotopologues. Values are given for the relevant irreducible representations of the molecular symmetry groups. These factors are applied in partition function calculations and line intensity normalisation.

			$g_{\text{ns}}$					
$\Gamma$	p/o	p	626	636	828	838	727	737
$A_1$	para	1	1	2	1	2	15	30
$A_2$	para	-1	1	2	1	2	15	30
$B_1$	ortho	-1	0	0	0	0	21	42
$B_2$	ortho	1	0	0	0	0	21	42
$\Gamma$			627	637	628	638	728	738
$A'$		1	6	12	1	2	6	12
$A''$		-1	6	12	1	2	6	12

leaving only  $A_1$  and  $A_2$ , which correlate with  $e/f$  parity according to:

$$e : (-1)^J = 1, \quad A_1, \quad (1)$$

$$e : (-1)^J = -1, \quad A_2, \quad (2)$$

$$f : (-1)^{J+1} = 1, \quad A_2, \quad (3)$$

$$f : (-1)^{J+1} = -1, \quad A_1. \quad (4)$$

For symmetric CO<sub>2</sub> with non-zero oxygen nuclear spin, all four irreps ( $A_1$ ,  $A_2$ ,  $B_1$ ,  $B_2$ ) are allowed. These can be correlated with ortho and para spin symmetries as summarised in Table 1. For the  $e/f$  labels, the convention  $p = (-1)^J$  for  $e$  and  $p = (-1)^{J+1}$  for  $f$  is applied, where  $p$  denotes molecular parity.

For asymmetric isotopologues, the rovibrational states transform as  $A'$  or  $A''$  in the  $C_s(M)$  group. Their relation to  $e/f$  parity follows the same rules as in the symmetric, zero-spin case:

$$e : (-1)^J = 1, \quad A', \quad (5)$$

$$e : (-1)^J = -1, \quad A'', \quad (6)$$

$$f : (-1)^{J+1} = 1, \quad A'', \quad (7)$$

$$f : (-1)^{J+1} = -1, \quad A'. \quad (8)$$

### 2.3 Selection rules

Rotational selection rules for linear molecules are  $\Delta J = 0, \pm 1$ . For CO<sub>2</sub>, Q-branch transitions ( $\Delta J = 0$ ) occur only in parallel bands and involve  $e \leftrightarrow f$  transitions, where the dipole moment change is parallel to the molecular axis. P- and R-branch transitions ( $\Delta J = \pm 1$ ) occur in both parallel and perpendicular bands and involve  $e \leftrightarrow e$  or  $f \leftrightarrow f$ .

For symmetric isotopologues with non-zero oxygen nuclear spin, additional nuclear-spin selection rules apply:

$$\text{ortho} \leftrightarrow \text{ortho}, \quad \text{para} \leftrightarrow \text{para}.$$

In terms of molecular symmetry, these correspond to

$$A_1 \leftrightarrow A_2, \quad B_1 \leftrightarrow B_2.$$

For asymmetric isotopologues, the  $e/f$  selection rule is general for all dipole allowed transitions and therefore still holds; in group-theoretical notation it is expressed as

$$A' \leftrightarrow A''.$$

The nuclear-spin degeneracy factors for the isotopologues considered in this work are summarised in Table 1.

### 3 LINE LIST PRODUCTION

The generation of high-quality line lists requires three key ingredients: (i) accurate PES and DMS to describe molecular structure and transition intensities; (ii) robust nuclear-motion calculations to solve the rovibrational Schrödinger equation; and (iii) empirical refinement procedures to bring calculated energy levels into agreement with experimental data. In this section we outline the methodology adopted for CO<sub>2</sub> isotopologues, including the choice of potential and dipole moment surfaces, the details of the variational calculations, and the empirical corrections applied to improve the accuracy of the final line lists.

### 3.1 Potential Energy Surface

We initially considered using the more recent empirical PES Ames-X01d of CO<sub>2</sub> developed by Huang et al. (2023), which was optimised to treat all isotopologues on an equal footing. The earlier PES, Ames-2 (Huang et al. 2017), originally developed for the main isotopologue <sup>12</sup>C<sup>16</sup>O<sub>2</sub>, was also available and had previously been used to construct the UCL-4000 line list (Yurchenko et al. 2020). However, our tests suggested that the optimisation in Ames-X01d came at the cost of somewhat degraded line list quality. For <sup>12</sup>C<sup>16</sup>O<sub>2</sub> and <sup>13</sup>C<sup>18</sup>O<sub>2</sub>, this is illustrated in Fig. 1, which compares TROVE-calculated term values with experimentally derived values (MARVEL or CDS-2024-PI (Kochanov & Perevalov 2025)) using both PESs. Ames-2 provides a more compact and flatter  $J$ -dependence, indicating more accurate equilibrium values and greater suitability for subsequent band-centre corrections. Our tests confirmed this trend across all 12 isotopologues, with Ames-2 consistently giving better agreement with MARVEL and HITRAN energies, at least using TROVE. We therefore adopted Ames-2 for all line lists reported in this work.

### 3.2 Dipole Moment Surface

For transition intensities we used the *ab initio* DMS Ames-2021-40K of CO<sub>2</sub> by Huang et al. (2023), the latest in the Ames series of dipole moment surfaces. In our previous line list, UCL-4000, the DMS of Polyansky et al. (2015) was employed.

### 3.3 Variational nuclear-motion calculations

The rovibrational Schrödinger equation was solved using the program TROVE (Yurchenko et al. 2007). Our methodology follows Yurchenko & Mellor (2020) and Yurchenko et al. (2024), employing the exact KEO in the bisector frame together with basis functions constructed from associated Laguerre polynomials. For full details the reader is referred to these works; here we summarise only the main steps.

First, vibrational  $J = 0$  eigenfunctions  $\Psi_{\lambda,L}^{(J=0,\Gamma_{\text{vib}})}$  were obtained variationally for  $L = 0 \dots L_{\text{max}}$  by diagonalising the  $J = 0$  Hamiltonian  $\hat{H}^{(J=0)}$  in all relevant irreducible representations ( $A_1, A_2, B_1, B_2$  or  $A', A''$  for symmetric or asymmetric species, respectively). The primitive basis was constructed as a product of 1D vibrational functions  $\phi_{n_1}(r_1)$ ,  $\phi_{n_2}(r_2)$ , and  $\phi_{n_3}^L(\rho)$ , where  $r_1$  and  $r_2$  are stretching coordinates and  $\rho = \pi - \alpha$  with  $\alpha$  the bond angle (Yurchenko & Mellor 2020).

For  $J > 0$ , rovibrational basis functions were formed as contracted, symmetrised products of the  $J = 0$  vibrational functions and rigid-rotor functions:

$$\Psi_{\lambda,K}^{(J,\Gamma)} = \{\Psi_{\lambda,K}^{(J=0,\Gamma_{\text{vib}})} |J, K, \Gamma_{\text{rot}}\}^{\Gamma}, \quad (9)$$

where  $|J, K, \Gamma_{\text{rot}}\rangle$  are symmetrised rigid-rotor functions (Yurchenko et al. 2017),  $K$  is constrained by  $L$  ( $K = L$ ), and  $\Gamma, \Gamma_{\text{vib}}, \Gamma_{\text{rot}}$  are the total, vibrational, and rotational symmetries in  $C_{2v}(\text{M})$  or  $C_s(\text{M})$ . Nuclear masses adopted were:  $m_{\text{C}} = 11.99670909 \text{ Da}$  (<sup>12</sup>C) and  $13.000063355 \text{ Da}$  (<sup>13</sup>C);  $m_{\text{O}} = 15.990525980 \text{ Da}$  (<sup>16</sup>O),  $16.99474312 \text{ Da}$  (<sup>17</sup>O), and  $17.99477097 \text{ Da}$  (<sup>18</sup>O).

Rovibrational wavefunctions were computed up to  $J_{\text{max}}$  (see Table 2) and used to generate transition intensities for all dipole-allowed transitions. For <sup>12</sup>C<sup>16</sup>O<sub>2</sub>, lower and upper state energies were limited to  $16\,000 \text{ cm}^{-1}$  and  $36\,000 \text{ cm}^{-1}$ , respectively. For <sup>13</sup>C<sup>16</sup>O<sub>2</sub>, the lower-state energy cut-off was set to  $12\,000 \text{ cm}^{-1}$ . For all other isotopologues the lower-state cut-off was  $10\,000 \text{ cm}^{-1}$ . Transition wavenumbers spanned  $0\text{--}20\,000 \text{ cm}^{-1}$ . Nuclear spin statistical weights  $g_{\text{ns}}$  for all isotopologues are given in Table 1.

### 3.4 Empirical corrections of $J = 0$ energies

To improve calculated rovibrational energies, empirical band-centre corrections (EBCC) (Yurchenko et al. 2009, 2011) were applied to the diagonal elements of the  $J = 0$  Hamiltonian matrices. These corrections were obtained as average residuals between TROVE-calculated  $J = 0$  band origins and empirical values (from MARVEL, CDS-2024-PI, or HITRAN2020). For <sup>12</sup>C<sup>16</sup>O<sub>2</sub>, the procedure is illustrated in Fig. 2.

Since  $J = 0$  basis functions are eigenfunctions of the vibrational Hamiltonian, their diagonal elements can be straightforwardly replaced by empirical energies, thereby propagating improvements to higher- $J$  rovibrational levels (Yurchenko et al. 2009; Mant et al. 2018). These also include states with  $\ell_2 > 0$ , which formally do not exist in Nature but are present in the basis set. This significantly reduced obs.-calc. residuals across most isotopologues. The exception was <sup>16</sup>O<sup>12</sup>C<sup>18</sup>O, where some bands diverged at high  $J$  after EBCC (Fig. 2, green crosses). For this isotopologue, band-centre shifts were not applied.

### 3.5 MARVELisation procedure

Further improvements were made using the hybrid MARVELisation approach (McKemmish et al. 2024), in which calculated energies are replaced, where available, by more accurate values derived from MARVEL or effective Hamiltonian (EH) analyses.

**Table 2.** Summary of CO<sub>2</sub> isotopologue line lists.  $L_{\max}$  is the maximum vibrational angular momentum;  $J_{\max}$  the maximum rotational quantum number;  $E''_{\max}$  the maximum lower-state energy;  $N_{\text{state}}$  the number of states in the ExoMol .states file;  $N_{\text{lines}}$  the number of transitions in the .trans file;  $N_{\text{HI}}$  the number of HITRAN lines at  $T = 296$  K;  $N_{\text{Ca}}$  the number of calculated ExoMol lines at  $T = 296$  K;  $N_{\text{Ma}}$  the number of substituted lines with MARVEL values at  $T = 296$  K;  $N_{\text{Ma+HI}}$  the total number of ‘MARVELised’ lines (Ma/HI or EH) at  $T = 296$  K; and the terrestrial isotopic abundance from HITRAN (Gordon et al. 2022) is given in the final column. Only transitions stronger than  $I = 10^{-30}$  cm/molecule at  $T = 296$  K are counted.

Iso	$L_{\max}$	$J_{\max}$	$E''_{\max}$ (cm <sup>-1</sup> )	$N_{\text{state}}$	$N_{\text{lines}}$	$N_{\text{HI}}$ 296 K	$N_{\text{Ca}}$ 296 K	$N_{\text{Ma}}$ 296 K	$N_{\text{Ma+HI}}$ 296 K	Abundance (HITRAN)
626	30	250	16000	3 646 814	3 607 555 029	175891	174445	175109	175109	$9.8420 \times 10^{-1}$
627	10	150	10000	5 065 351	1 042 026 128	73221	72228	36582	73082	$7.3399 \times 10^{-4}$
628	20	150	10000	7 369 500	1 112 362 652	116222	118701	58841	115774	$3.9471 \times 10^{-3}$
636	30	150	12000	2 670 885	753 056 397	70884	69870	38525	70779	$1.1057 \times 10^{-2}$
637	10	150	10000	7 026 133	1 169 286 790	22830	22577	4572	22812	$8.2462 \times 10^{-6}$
638	10	150	10000	4 072 374	1 246 979 498	40304	39950	12592	40240	$4.4345 \times 10^{-5}$
727	20	150	10000	5 168 133	583 350 654	6558	6493	5372	6551	$1.3685 \times 10^{-7}$
728	16	150	10000	6 897 362	1 141 805 035	5031	14378	4186	5030	$1.3685 \times 10^{-7}$
737	20	150	10000	5 133 983	92 365 743	1639	1501	903	1533	$1.5375 \times 10^{-9}$
738	10	150	10000	7 432 457	1 273 579 199	3580	3569	1288	3578	$1.6535 \times 10^{-8}$
828	20	150	10000	2 527 339	321 570 612	10541	1049	6267	10520	$3.9573 \times 10^{-6}$
838	20	150	10000	2 721 734	361 867 203	3053	2926	1146	2966	$4.4460 \times 10^{-8}$

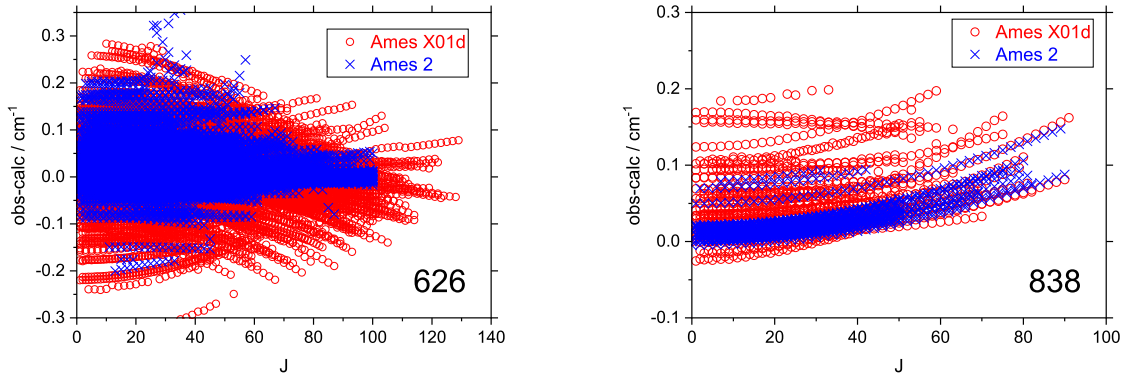


**Figure 1.** Obs.-Calc. residuals for  $^{12}\text{C}^{16}\text{O}_2$  and  $^{13}\text{C}^{18}\text{O}_2$  using two Ames PESs, Ames-2 (Huang et al. 2017), shown with red circles, and Ames-X01d (Huang et al. 2023), shown with blue crosses.

MARVEL energies were taken from the recent MARVEL studies of CO<sub>2</sub> isotopologues (Ibrahim et al. 2024; Alatoom et al. 2024; Azzam et al. 2024, 2025a,b; Obaidata et al. 2025; Mansour et al. 2025; Azzam et al. 2025c), while effective Hamiltonian energies were taken from CDSD-2024-PI (Kochanov & Perevalov 2025) ( $^{12}\text{C}^{16}\text{O}_2$ ) and HITRAN2020 (Gordon et al. 2022) (all minor isotopologues). The EH energies are used to minimise gaps in available MARVEL energy levels.

To this end, the EH energies were generated using the MARVEL algorithm applied to HITRAN transitions (Furtenbacher et al. 2007; Tobias et al. 2020; Arendas et al. 2020, 2024). The HITRAN uncertainty were set based on the corresponding HITRAN error code (Gordon et al. 2022), for example, for code 4 ( $0.0001 \text{ cm}^{-1} \leq \epsilon < 0.001 \text{ cm}^{-1}$ ), the uncertainty of  $0.0005 \text{ cm}^{-1}$  was assumed. For the main isotopologue  $^{12}\text{C}^{16}\text{O}_2$ , the CDSD-2024-PI energies were readily provided by Kochanov & Perevalov (2025). The MARVEL procedure ensures self-consistency of the derived network, with uncertainties propagated through the bootstrap algorithm (Tennyson et al. 2024a). While MARVEL is usually applied to directly measured transitions, here it is used on effective Hamiltonian-derived frequencies to supplement the empirical dataset.

In the ExoMol states files, purely MARVEL-derived levels are labelled “Ma”, HITRAN-derived levels as “HI”, and effective Hamiltonian values as “EH” (see the description of the hybrid MARVELisation approach of McKemmish et al. (2024)). For the main isotopologue  $^{12}\text{C}^{16}\text{O}_2$ , MARVEL data from Azzam et al. (2025a) were supplemented by CDSD-2024-PI (Kochanov & Perevalov 2025). The HITRAN energies generated using the MARVEL approach are provided as part of the supplementary material.

Table 2 also compares the number of lines for each isotopologue with a transition intensity greater than  $10^{-30}$  cm/molecule at 296 K. For some reason which remains unclear, given that our computed line lists are complete, HITRAN contains slightly more lines for each isotopologue.

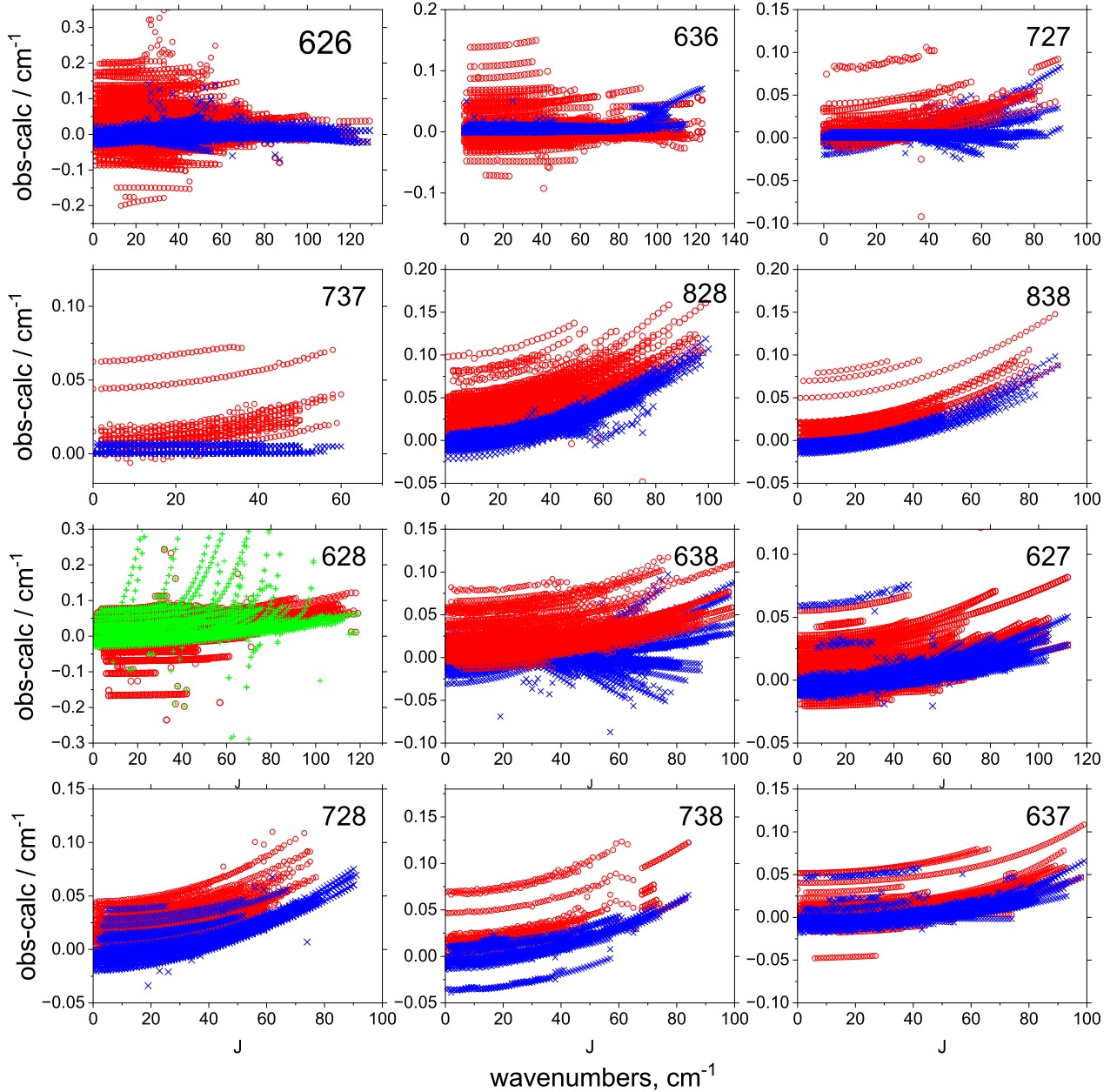


**Figure 2.** ‘Obs.-calc.’ residuals for different isotopologues using two Ames PESs, Ames-2 (Huang et al. 2017) and Ames-X01d (Huang et al. 2023), before (red circles) and after (blue crosses) the band centre corrections (Yurchenko et al. 2009). The green crosses in the display 628 show the divergence of the band-centre-corrected energies with  $J$  increases (see text).

#### 4 ROVIBRATIONAL LINE LISTS FOR CO<sub>2</sub> ISOTOPOLOGUES

Using the TROVE rovibrational wavefunctions and the *ab initio* DMS Ames-2021-40K, we generated 12 line lists for CO<sub>2</sub> isotopologues, collectively referred to as Dozen, in the ExoMol format (Tennyson et al. 2024b). The coverage extends from 0 to 20 000 cm<sup>-1</sup> (i.e. wavelengths  $\geq 0.5$   $\mu$ m). For the parent and most important isotopologue, <sup>12</sup>C<sup>16</sup>O<sub>2</sub>, we adopted a more extensive coverage of state excitations: a higher lower-state energy cut-off  $E''_{\max}$  of 16 000 cm<sup>-1</sup> (cf. 10 000–12 000 cm<sup>-1</sup> for other isotopologues). A larger  $E''_{\max}$  increases computational cost but improves population coverage of excited states and thus yields a larger, more complete line list (see Table 2). Further control of the excitation coverage is provided by  $J_{\max}$  and  $L_{\max}$ , which were selected per isotopologue (Table 2). The choice of  $L_{\max}$  affects the size of the basis set and thus its quality.

Each line list comprises a `.states` file, a set of `.trans` files, and a partition-function file `.pf`. As an example, an extract from the <sup>12</sup>C<sup>16</sup>O<sub>2</sub> `.states` file is given in Table 3. It contains state term values  $\bar{E}_i$ , total degeneracies  $g_i$ , uncertainties (unc),

lifetimes, and quantum numbers. Vibrational labels are provided in three conventions: Herzberg ( $v_1, v_2^{\ell_2}, v_3$ ), AFGL ( $m_1, m_2, l_2, m_3, r$ ), and TROVE local-mode indices ( $n_1, n_2, n_3, L$ ). Both rotationless parity ( $e/f$ ) and molecular symmetry ( $A_1, A_2, B_1, B_2, A', A''$ ) are provided. States are indexed by an integer  $i$  (state ID), used in the transition files.

The `.states` files are MARVELised: where available, calculated term values are replaced by empirical values, MARVEL (**Ma**), HITRAN (**HI**) or effective-Hamiltonian (CDS; **EH**), with the label supplied in the penultimate column; the original calculated value is retained in the final column. State-dependent lifetimes computed with Dozen are included (column 6; see Table 3).

For practicality, each isotopologue's transition set is divided into 20 `.trans` files, each covering a  $1000 \text{ cm}^{-1}$  bin over 0–20 000  $\text{cm}^{-1}$ . An extract from a  $^{12}\text{C}^{16}\text{O}_2$  `.trans` file is shown in Table 4, listing Einstein A coefficients and the upper/lower state IDs.

#### 4.1 Using machine learning to reconstruct spectroscopic quantum numbers

In order to help with the usage of the Dozen line list, quantum numbers for all three assignment schemes are provided as part of the States file. While the TROVE quantum numbers are generated using the largest contribution to the associated eigenfunctions, to assign vibrational quantum numbers for AFGL and Herzberg they are not known, we developed a machine learning (ML) pipeline. To this end, a classifier was implemented in Pytorch (Paszke et al. 2019) using a multi-head neural network architecture containing a shared backbone and specialized output heads.

The ML model starts with a shared feature extraction network consisting of 6 fully connected layers ( $512 \rightarrow 256 \rightarrow 128 \rightarrow 128 \rightarrow 64$  neurons) with GELU activations and dropout regularization to learn common representations from 32 molecular features (energy, quantum numbers, dipole moments, isotopic masses, symmetries). From the 64-dimensional shared representation, 8 separate classification heads branch out, each containing 3 additional layers ( $64 \rightarrow 32 \rightarrow$  output classes) to predict the specific quantum numbers (Herzberg:  $v_1, v_2, l_2$ , and  $v_3$  and AFGL:  $m_1, m_2, m_3$ , and  $r$ ). This design enables the backbone to capture shared molecular physics, while each head specializes in its respective quantum-number assignment task. Crucially, we enforce quantum-mechanical constraints within the loss function, limiting  $l_2$  values according to the parity of  $v_2$ .

We assess model uncertainty using Monte Carlo (MC) Dropout (Gal & Ghahramani 2016), which keeps dropout layers active during inference by effectively sampling multiple network realizations. We perform 50 forward passes per sample, obtaining a distribution of class probabilities. From the mean probability vector  $\bar{p}$ , we compute predictive entropy:  $H(\bar{p}) = -\sum \bar{p} \log \bar{p}$ , normalized to  $[0, 1]$  by dividing by  $\log(n_{\text{classes}})$ . A normalized entropy threshold of 0.4, determined from prior validation to optimize the trade-off between accepted correct predictions and rejected incorrect ones, was applied. Predictions below this threshold were accepted, enabling the assignment of over one million spectral lines across all targeted isotopologues.

For different isotopologues, the ML procedure resulted in 80 000–120 000 states additionally assignments with AFGL and Herzberg. While this represents only 1.4–3% of the total number of states in each data set, this is a multifold increase comparing to the empirically assignment states, which is illustrated in Fig. 3.

#### 4.2 Partition functions

Partition functions were computed for all 12 isotopologues on a 1 K grid from 0 to 5000 K using the direct sum

$$Q(T) = \sum_i g_{\text{ns}}^{(i)} (2J_i + 1) \exp\left(-\frac{c_2 \tilde{E}_i}{T}\right),$$

where  $g_{\text{ns}}^{(i)}$  is the nuclear-spin statistical factor (Table 1),  $J_i$  is the rotational quantum number,  $c_2$  is the second radiation constant ( $\text{cm K}$ ), and  $\tilde{E}_i$  is the energy term value ( $\text{cm}^{-1}$ ) relative to the ground state ( $J = 0, v_1 = v_2 = v_3 = 0, \ell_2 = 0, e$ ).

Figure 4 compares the Dozen partition function for  $^{12}\text{C}^{16}\text{O}_2$  with TIPS 2024 (total internal partition sum) of HITRAN2020 (Gamache et al. 2025) and with that obtained from the Ames AI-3000K line list (Huang et al. 2023). The Dozen and Ames curves agree closely and both lie systematically above the HITRAN TIPS values, reflecting improved completeness of the underlying states; the lack of convergence of the HITRAN TIPS partition function at high temperature has been noted previously (Wang et al. 2023).

#### 4.3 Opacities

Temperature- and pressure-dependent opacities for all 12 isotopologues of  $\text{CO}_2$ , based on the Dozen line lists, were generated using the ExoMolOP procedure (Chubb et al. 2021). Opacity tables were produced for four widely used atmospheric retrieval codes: ARCIS (Min et al. 2020), TAUREX (Al-Refaie et al. 2021), NEMESIS (Irwin et al. 2008), and PETITRADTRANS (Mollière et al. 2019), and are provided alongside the line lists. In addition, we supply combined opacities constructed for a representative atmosphere containing multiple isotopologues in terrestrial abundance ratios (see Table 2).

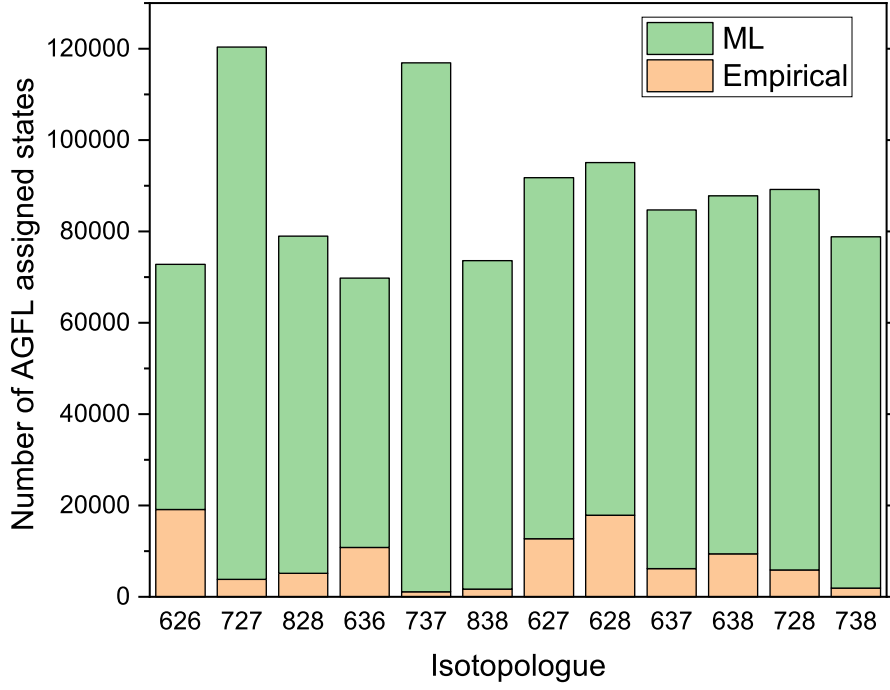


**Figure 3.** Coverage of the assigned states with the AFGL quantum numbers per isotopologue comparing to the corresponding empirical assignments: MARVEL, HITRAN or CDSD-2024-PI.

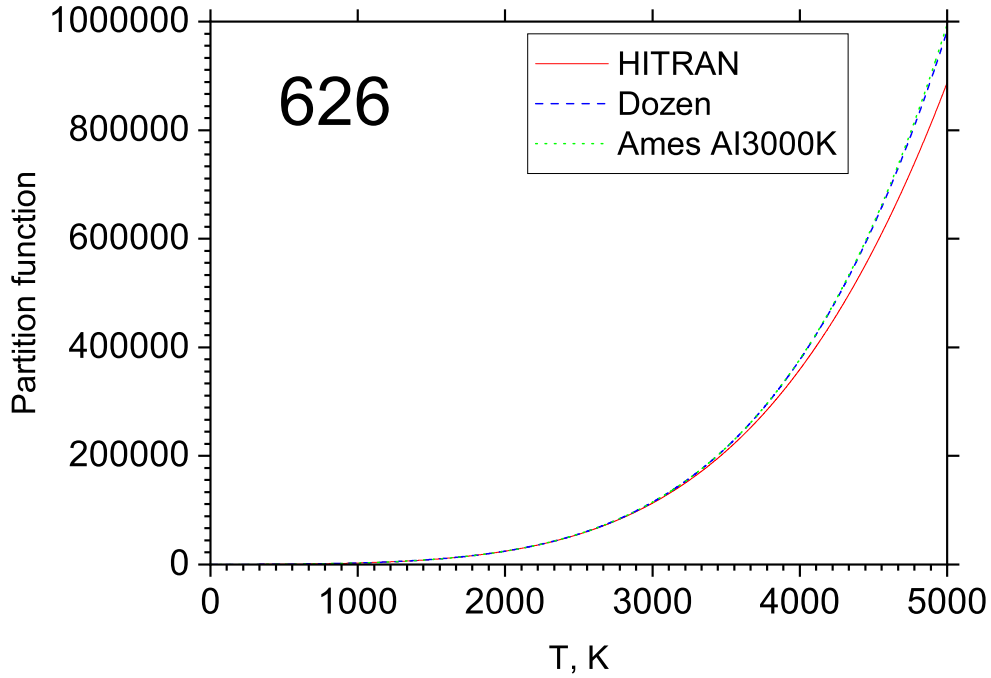


**Figure 4.** Partition functions for  $^{12}\text{C}^{16}\text{O}_2$ : comparison of Dozen with TIPS 2024 of HITRAN2024 (Gamache et al. 2025) and Ames AI-3000K.

**Table 3.** Extract from the `.states` file of  $^{12}\text{C}^{16}\text{O}_2$  Dozen line list.

$i$	$\tilde{E}/\text{cm}^{-1}$	$g$	$J$	$\text{unc}/\text{cm}^{-1}$	$\tau/\text{s}$	$\Gamma_{\text{tot}}$	$e/f$	$v_1$	$v_2$	$v_3$	$ C_i^2 $	$m_1$	$m_2$	$l_2$	$m_3$	$r$	$n_1$	$n_2$	$n_3$	Label	$\tilde{E}_{\text{calc.}}/\text{cm}^{-1}$
1	0.000000	1	0	0.000001	inf	A1	e	0	0	0	0 1.00	0	0	0	0	1	0	0	0	Ma	0.000000
2	1285.408294	1	0	0.000049	7.7985E-01	A1	e	0	2	0	0 0.54	1	0	0	0	2	0	0	1	Ma	1285.407001
3	1388.184102	1	0	0.000053	5.5304E-01	A1	e	1	0	0	0 0.54	1	0	0	0	1	1	0	0	Ma	1388.184019
4	2548.363900	1	0	0.001515	3.5601E-01	A1	e	1	2	0	0 0.47	2	0	0	0	3	1	0	1	Ma	2548.364344
5	2671.143088	1	0	0.001119	4.8854E-01	A1	e	2	0	0	0 0.66	2	0	0	0	2	1	1	0	Ma	2671.142828
6	2797.136399	1	0	0.001000	2.3234E-01	A1	e	1	2	0	0 0.52	2	0	0	0	2	1	0	1	EH	2797.135151
7	3792.682402	1	0	0.001000	2.3664E-01	A1	e	1	4	0	0 0.43	3	0	0	0	3	1	0	2	EH	3792.680795
...	...	...	...	...	...	...	...	...	...	...	...	...	...	...	...	...	...	...	...	...	...
18	6016.690108	1	0	0.001000	1.2107E-03	A1	e	1	0	0	2 0.60	1	0	0	2	0	0	3	0	EH	6016.701190
19	6240.057942	1	0	0.080000	1.5052E-01	A1	e	2	6	0	0 0.30	5	0	0	0	4	1	1	3	Ca	6240.057942
20	6435.500064	1	0	0.060000	1.7500E-01	A1	e	4	2	0	0 0.28	5	0	0	0	4	2	2	1	Ca	6435.500064
21	6588.319980	1	0	0.050000	2.2609E-01	A1	e	5	0	0	0 0.48	5	0	0	0	2	3	2	0	Ca	6588.319980
...	...	...	...	...	...	...	...	...	...	...	...	...	...	...	...	...	...	...	...	...	...
30	7834.845932	1	0	0.040000	1.7933E-01	A1	e	1	0	0	3 0.29	-1	-1	-1	-1	-1	2	2	0	Ca	7834.845932
31	7974.351788	1	0	0.040000	1.7354E-01	A1	e	1	0	0	3 0.51	-1	-1	-1	-1	-1	2	2	0	Ca	7974.351788

$i$ :	State identifier (integer index used in <code>.trans</code> files).
$\tilde{E}$ :	State term value ( $\text{cm}^{-1}$ ).
$g$ :	Total state degeneracy.
$J$ :	Total rotational quantum number.
$\text{unc}$ :	Energy uncertainty ( $\text{cm}^{-1}$ ).
$\tau$ :	State lifetime (s).
$\Gamma_{\text{tot}}$ :	Total symmetry in $C_{2v}(\text{M})$ or $C_s(\text{M})$ .
$e/f$ :	Rotationless parity label.
$v_1, v_2^{\ell_2}, v_3$ :	Normal-mode vibrational quantum numbers (Herzberg notation).
$ C_i ^2$ :	Largest expansion-coefficient weight used for assignment.
$m_1, m_2, l_2, m_3, r$ :	AFGL vibrational quantum numbers ( $-1$ stands for non-available).
$n_1, n_2, n_3, L$ :	TROVE local-mode quantum numbers.
Label:	MARVEL (Ma), Effective Hamiltonian (EH), HITRAN (HI), or calculated Dozen value (Ca).
$\tilde{E}_{\text{calc.}}$ :	Original calculated Dozen term value ( $\text{cm}^{-1}$ ).

**Table 4.** Extract from a `.trans` file of the  $^{12}\text{C}^{16}\text{O}_2$  Dozen line list.

$f$	$i$	$A_{fi}$
872090	849449	3.7641e-16
1729336	1740374	1.9742e-09
443590	423498	2.7506e-15
89228	95628	1.9493e-12
1562467	1577182	1.1399e-08
1031039	1081028	3.1880e-14
1710529	1691051	4.1274e-14
2476483	2488556	1.5718e-09
1139554	1151915	5.3921e-11
1726661	1675412	4.8961e-11

$f$ : Upper state counting number;  
 $i$ : Lower state counting number;  
 $A_{fi}$ : Einstein A coefficient (in  $\text{s}^{-1}$ ).

#### 4.4 Line broadening coefficients

Accurate treatment of collisional line broadening is essential for radiative-transfer modelling. We adopt a semi-empirical approach, combining theoretical predictions with carefully selected experimental data, to provide broadening and shifting coefficients for  $\text{CO}_2$  transitions with common perturbers ( $\text{N}_2$ ,  $\text{O}_2$ ,  $\text{CO}_2$ ,  $\text{H}_2$ ,  $\text{He}$ , and  $\text{H}_2\text{O}$ ) over the temperature range 200–2000 K.

Previous analyses have highlighted inconsistencies among experimental datasets. For example, [Gamache & Lamouroux \(2013\)](#) and [Gamache et al. \(2014\)](#) showed that different experiments on the same transition often disagree beyond the quoted uncertainties, complicating attempts to assess vibrational or isotopologue dependences of the half-width coefficients  $\gamma$ . More recent work by [Hashemi et al. \(2020\)](#) re-analysed the most reliable data, proposing a new set of semi-empirical parameters for

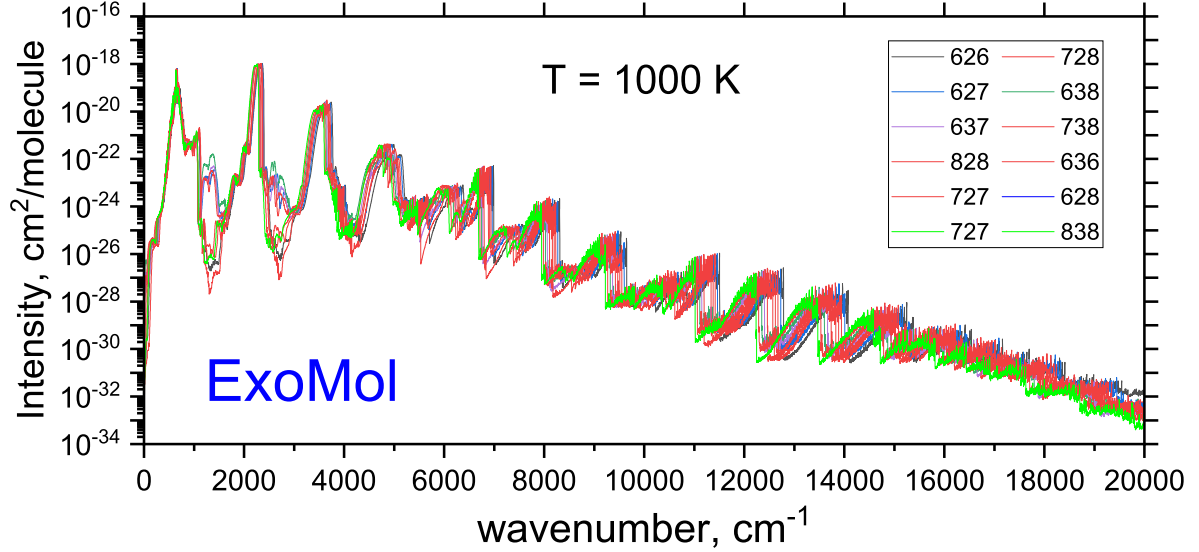


**Figure 5.** Spectra of CO<sub>2</sub> isotopologues at  $T = 1000$  K (Gaussian profile, HWHM =  $1 \text{ cm}^{-1}$ ). Intensities are not scaled to isotopic abundances.

CO<sub>2</sub>- and air-broadening, suitable for Voigt and speed-dependent Voigt profiles, and found no significant vibrational dependence of  $\gamma_0$ .

Isotopologue effects are also small. For example, [Devi et al. \(1998\)](#) found no statistically significant difference between N<sub>2</sub>-broadening of <sup>16</sup>O<sup>13</sup>C<sup>18</sup>O and that of the main isotopologue, while [Gamache & Lamouroux \(2013\)](#) estimated that isotopic mass effects reduce  $\gamma$  by less than 1%. This was recently confirmed by cavity ringdown measurements of <sup>13</sup>C<sup>16</sup>O<sub>2</sub> by [Mondelain et al. \(2025\)](#), who found air-broadening coefficients only 0.4% smaller than those of <sup>12</sup>C<sup>16</sup>O<sub>2</sub>.

Given the very weak vibrational and isotopologue dependences, we provide only  $J$ -dependent broadening coefficients  $\gamma_0$  (296 K) and temperature exponents  $n$  for the single power-law parametrisation. Speed dependence and line-mixing are not considered. The adopted  $\gamma_0$  and  $n$  values are taken from HITRAN for broadening by H<sub>2</sub>, He ([Tan et al. 2022](#)), N<sub>2</sub>, CO<sub>2</sub> ([Gordon et al. 2022](#)), and H<sub>2</sub>O ([Tan et al. 2019](#)), and are supplied in the m0-diet format for use with EXOCROSS ([Tennyson et al. 2024b](#)). In addition, we provide more recent theoretical water-broadening data ([Vispoel & Gamache 2024](#)) in the m2-diet format ([Sokolov et al. 2025](#)), which employs a double power-law to describe the temperature dependence of  $\gamma(T)$  more accurately.

## 5 ILLUSTRATIONS AND ANALYSIS

In this section we demonstrate the performance of the new line lists by comparing their predicted spectra with previous datasets and with available experimental information. A general overview is provided in Fig. 5, which shows spectra of all isotopologues at  $T = 1000$  K on a logarithmic scale, without scaling to isotopic abundances.

Figure 6 illustrates the coverage and quality of the Dozen <sup>12</sup>C<sup>16</sup>O<sub>2</sub> line list at  $T = 2000$  K, compared with our previous UCL-4000 list and the Ames AI-3000K list ([Huang et al. 2023](#)). The Dozen results are in excellent agreement with AI-3000K. We also compared with HITEMP 2025 ([Hargreaves et al. 2024](#)), which was generated from AI-3000K using the super-lines and super-energies technique ([Hargreaves et al. 2020](#)). As expected, the HITEMP spectrum follows AI-3000K closely over 0–12 000  $\text{cm}^{-1}$ , which is the range adopted by HITEMP for <sup>12</sup>C<sup>16</sup>O<sub>2</sub>.

Compared to UCL-4000, the new line list exhibits more physical behaviour at higher wavenumbers. This was achieved by optimising the stretching basis set comparing to that used in [Yurchenko et al. \(2020\)](#) by extending the bond-length grid used in the numerical integrations from 2.2 Å to  $\sim 2.6$  Å. The wavenumber behaviour of Dozen is now consistent with the near-integrated dipole limit (NIDL) ([Medvedev & Ushakov 2022](#); [Medvedev et al. 2020](#)), which predicts that overtone intensities decrease approximately exponentially, appearing as straight lines in a log-intensity plot ([Medvedev et al. 2016](#)). By contrast, the formation of plateaux at high overtones is a well-known indicator of numerical artefacts, as seen in UCL-4000 above 14 000  $\text{cm}^{-1}$ .

A more subtle intensity problem in UCL-4000 was identified by [Balashov et al. \(2024\)](#). Transitions in the 700 nm region ( $\sim 14\,300 \text{ cm}^{-1}$ ) were predicted with intensities above  $10^{-30} \text{ cm}^2/\text{molecule}$ , yet an extensive experimental search found no evidence for them. This band was therefore significantly overestimated in UCL-4000. The present line list, based on the

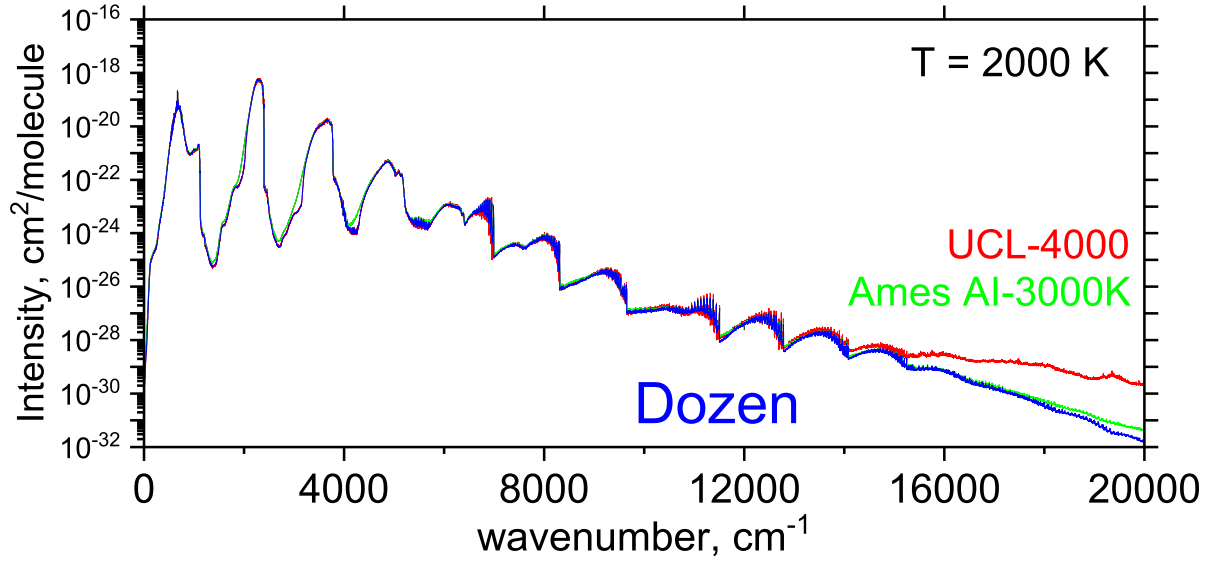


**Figure 6.** Cross-sections of  $^{12}\text{C}^{16}\text{O}_2$  at  $T = 2000$  K computed with UCL-4000, Dozen, AI-3000K, and HITEMP 2025 (Gaussian profile,  $\text{HWHM} = 1 \text{ cm}^{-1}$ ). The HITEMP 2025 and AI-3000K (Huang et al. 2023) spectra coincide over  $0\text{--}12\,000 \text{ cm}^{-1}$ .

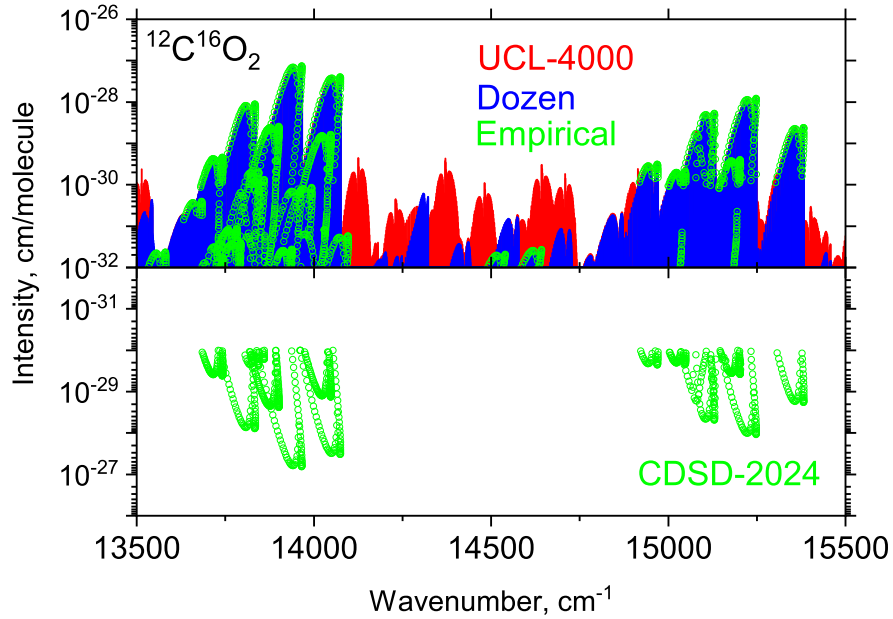


**Figure 7.** Intensity behaviour near  $700 \text{ nm}$  ( $\sim 14\,300 \text{ cm}^{-1}$ ). UCL-4000 overestimates this band, while the new Dozen list based on Ames-2021-40K yields significantly lower intensities, in better agreement with the experiment of Balashov et al. (2024).

improved basis set and different Ames-2021-40K DMS, brings these intensities below the  $10^{-30} \text{ cm molecule}^{-1}$  threshold value, as shown in Fig. 7.

Differences among isotopologues are illustrated in Fig. 8, which shows  $T = 296 \text{ K}$  spectra scaled by natural terrestrial abundances. Apart from the dominant  $^{12}\text{C}^{16}\text{O}_2$ , only  $^{13}\text{C}^{16}\text{O}_2$  and  $^{16}\text{O}^{12}\text{C}^{18}\text{O}$  produce IR features of sufficient strength to be detectable under atmospheric conditions. Of course, this situation will change with the altered isotope abundances encountered elsewhere in space.

Finally, Figures 9 and 10 present stick spectra at  $T = 296 \text{ K}$  for all 12 isotopologues of  $\text{CO}_2$ , separated into symmetric and asymmetric species. MARVELised transitions are highlighted, illustrating the extent of experimental coverage. Comparisons with HITRAN2020 (and CDSD-2024 for  $^{12}\text{C}^{16}\text{O}_2$ ) further demonstrate the accuracy and completeness of the new line lists.

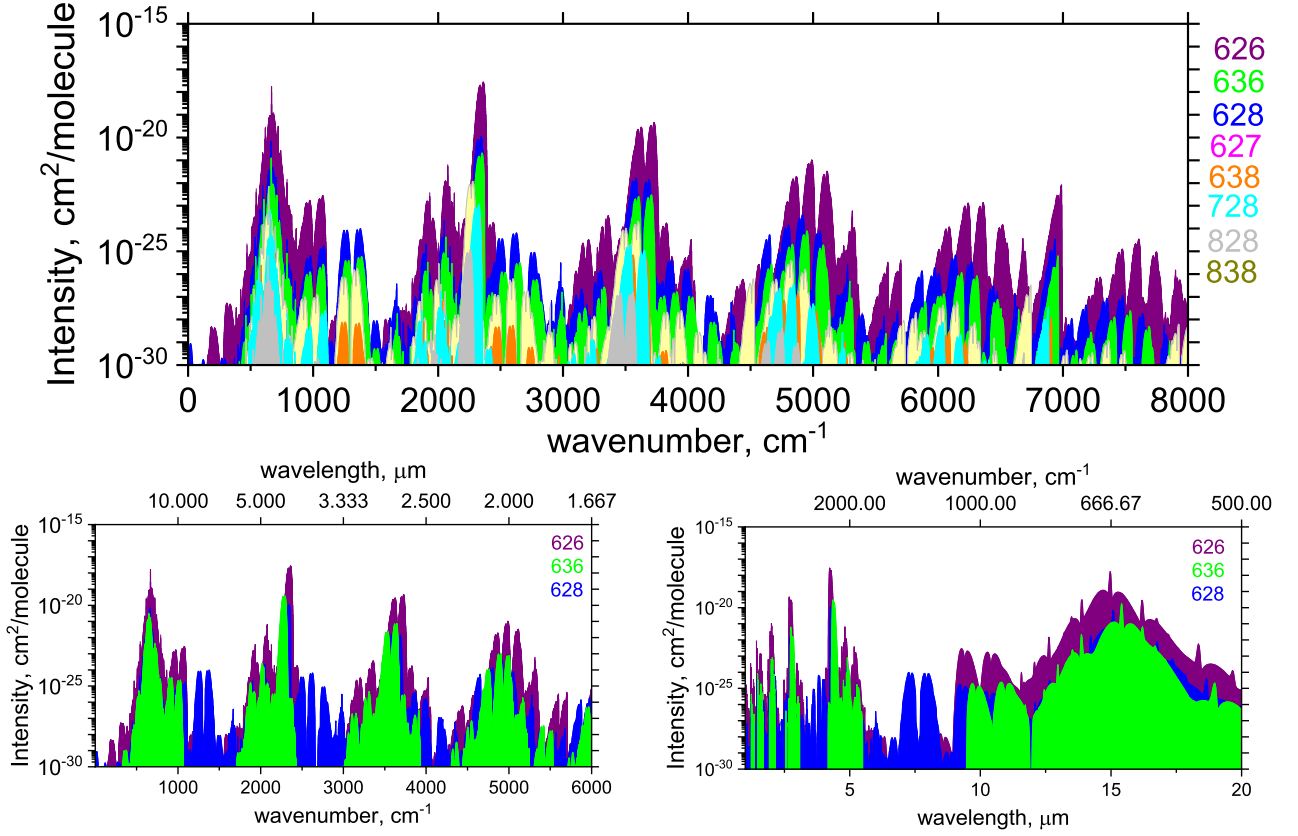


**Figure 8.** Spectra of selected CO<sub>2</sub> isotopologues at  $T = 296$  K, scaled by terrestrial isotopic abundances. In addition to  $^{12}\text{C}^{16}\text{O}_2$ , only  $^{13}\text{C}^{16}\text{O}_2$  and  $^{16}\text{O}^{12}\text{C}^{18}\text{O}$  produce detectable IR features.

A quantitative summary of line list statistics, including the number of empirically anchored transitions above the HITRAN intensity threshold of  $10^{-30}$  cm<sup>2</sup>/molecule at  $T = 296$  K, is given in Table 2.

## 6 CONCLUSIONS

This work presents a new set of comprehensive rovibrational line lists for 12 isotopologues of CO<sub>2</sub> collectively known as the Dozen line list. These line lists were computed using accurate empirical PESs and the latest *ab initio* DMSs from the Ames group (Huang et al. 2017, 2023), covering the spectroscopic range up to 20 000 cm<sup>-1</sup>. The line list for the main isotopologue  $^{12}\text{C}^{16}\text{O}_2$  is applicable up to at least 3000 K, while those for the minor isotopologues are reliable up to about 2000 K. The accuracy of the datasets has been enhanced through empirical band-centre corrections and systematic MARVELisation, incorporating experimental energies from MARVEL, HITRAN, and CDSD where available.

The new ExoMol CO<sub>2</sub> line lists represent a significant improvement over previous work. In particular, we now provide hot line lists for 12 isotopologues with an extended wavenumber coverage. Besides, spectra generated using Dozen display physically correct intensity behaviour for the high overtone bands thus avoiding the spurious plateau observed in UCL-4000 (Yurchenko et al. 2020). The intensity anomaly in the 700 nm region is resolved by improving the stretching basis set used. Comparisons with HITRAN spectra at  $T = 296$  K show excellent agreement, confirming both the reliability of line positions and the accuracy of intensities.

For the first time, we employed machine-learning methods to reconstruct AFGL and ‘Herzberg’ quantum numbers for CO<sub>2</sub> isotopologues, significantly extending the quantum assignment coverage in a consistent and physically constrained manner. We are currently using machine-learning techniques to improve the prediction transition wavenumbers for isotopologues (Barnfield et al. 2026); these results will be used to update Dozen states files for minor isotopologues with improved estimates for their energy levels in the near future. Partition functions have been computed on a fine temperature grid up to 5000 K, ensuring robust thermodynamic and opacity applications. Pressure-broadening coefficients with the most important perturbers (N<sub>2</sub>, O<sub>2</sub>, CO<sub>2</sub>, H<sub>2</sub>, He, H<sub>2</sub>O, and air) have been collected from the literature and are provided in ExoMol’s diet formats (m0 and m2), enabling flexible use in radiative-transfer models.

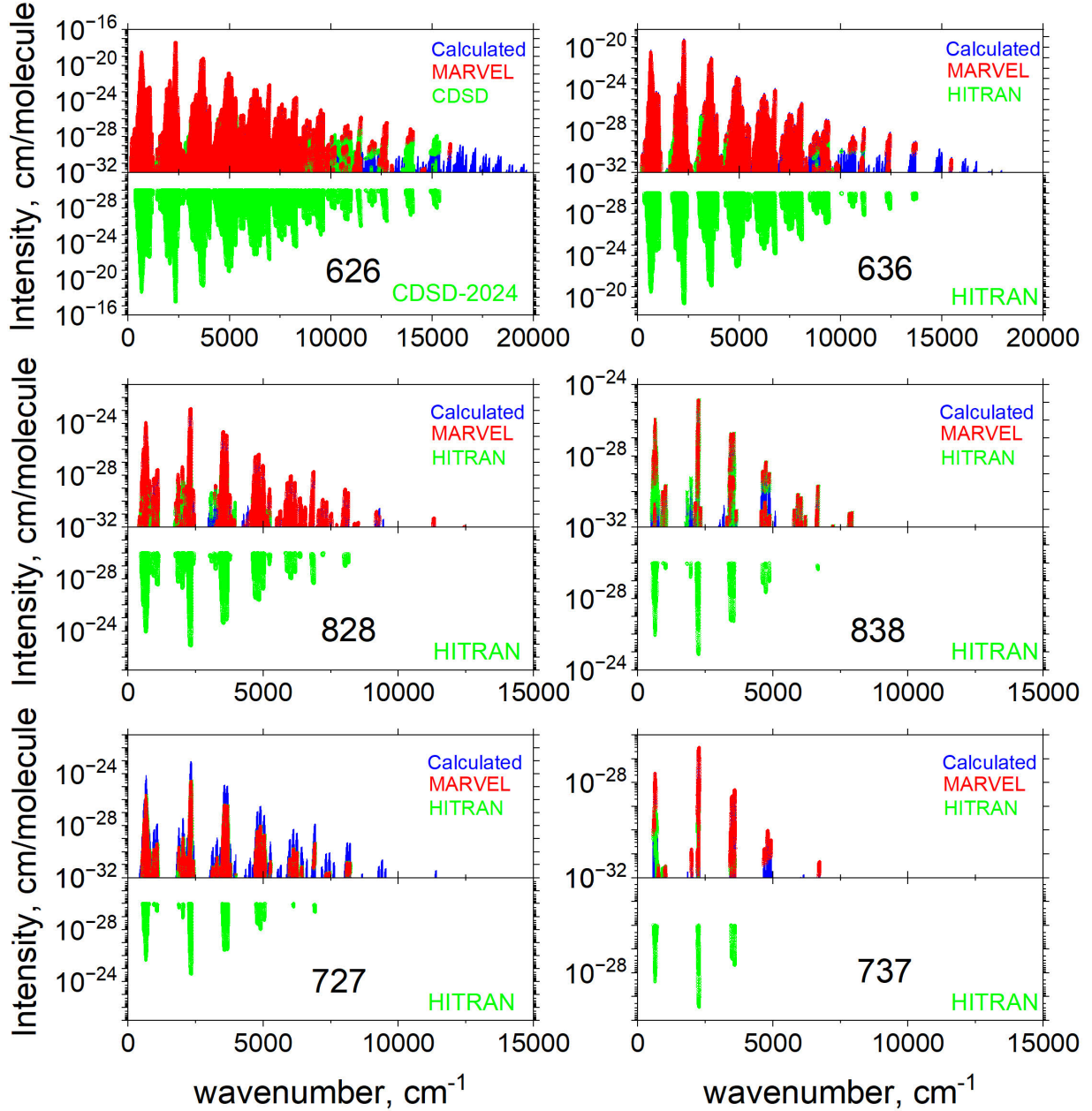


**Figure 9.** Stick spectra of six symmetric isotopologues of CO<sub>2</sub> at  $T = 296$  K (absorption coefficients in cm/molecule). MARVELised transitions are highlighted, and comparisons are made with CDSD-2024 (<sup>12</sup>C<sup>16</sup>O<sub>2</sub>) and HITRAN2020. Intensities are not scaled to isotopic abundances.

Opacities were generated with ExoMolOP (Chubb et al. 2021) for four leading atmospheric retrieval codes (ARCIS, TAUREX, NEMESIS, and PETITRADTRANS). Combined opacity grids, scaled to terrestrial isotopic abundances, are also supplied for practical applications in planetary and stellar atmosphere modelling.

The line lists and associated data (partition functions, broadening parameters, opacities) are available in the ExoMol database at [www.exomol.com](http://www.exomol.com). Together, they provide the most complete and accurate spectroscopic resource to date for CO<sub>2</sub> and its isotopologues. These datasets will be invaluable for atmospheric retrievals across the Solar System, brown dwarfs, and exoplanets, as well as for laboratory and terrestrial remote-sensing studies. Future work will focus on extending the spectral range into the ultraviolet and further refining high-temperature coverage.

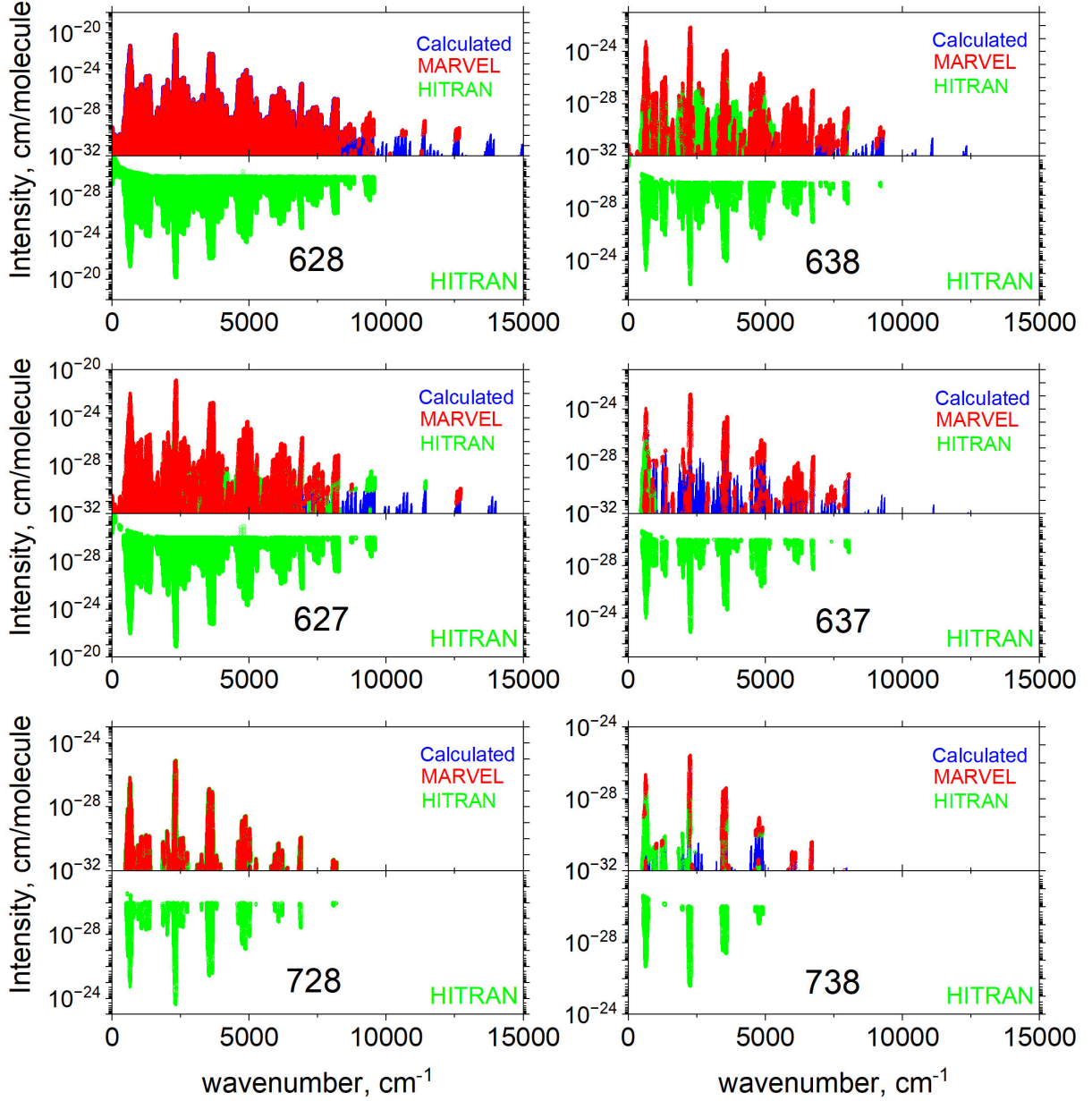


**Figure 10.** Stick spectra of six asymmetric isotopologues of CO<sub>2</sub> at  $T = 296$  K (absorption coefficients in cm/molecule). MARVELised transitions are highlighted and compared with HITRAN2020. Intensities are not scaled to isotopic abundances.

#### DECLARATION OF COMPETING INTEREST

The authors declare that they have no known competing financial interests or personal relationships that could have appeared to influence the work reported in this paper.

#### ACKNOWLEDGEMENTS

This work was supported by the STFC Projects ST/Y001508/1 and UKRI/ST/B001183/1. The authors acknowledge the use of the Cambridge Service for Data Driven Discovery (CSD3) and the DiRAC Data Intensive service DiAL2.5 at the University of Leicester, managed on behalf of the STFC DiRAC HPC Facility ([www.dirac.ac.uk](http://www.dirac.ac.uk)). These DiRAC services were funded by BEIS, UKRI and STFC capital funding and STFC operations grants. DiRAC is part of the UKRI Digital Research

Infrastructure. We thank Xinchuan Huang for help accessing AI-3000K and providing valuable suggestions. This work was also supported by the European Research Council (ERC) under the European Union’s Horizon 2020 research and innovation programme through Advance Grant number 883830.

## DATA AVAILABILITY

All data generated in this article are available in the article and its supplementary materials or via the the ExoMol website [www.exomol.com](http://www.exomol.com). The HITRAN energies of 11 minor isotopologues generated using the MARVEL procedure underlying this article are available in the online supplementary material. The line lists and associated data are available from [www.exomol.com](http://www.exomol.com). The codes used in this work, namely TROVE and EXOCROSS, are freely available via <https://github.com/exomol>.

## REFERENCES

- Abshire J. B., et al., 2010, in Singh U. N., Pappalardo G., eds, , Vol. 7832, Lidar Technologies, Techniques, and Measurements for Atmospheric Remote Sensing VI. SPIE, pp 72–84, [doi:10.1117/12.868567](https://doi.org/10.1117/12.868567), <https://doi.org/10.1117/12.868567>
- Ahrer E.-M., et al., 2023, *Nature*, 614, 649
- Al-Refaie A. F., Changeat Q., Waldmann I. P., Tinetti G., 2021, *ApJ*, 917, 37
- Alatoom D., Ibrahim M. T. I., Furtenbacher T., Császár A. G., Alghizzawi M., Yurchenko S. N., Azzam A. A. A., Tennyson J., 2024, *J. Comput. Chem.*, 45, 2558
- Amat G., Pimbert M., 1965, *J. Mol. Spectrosc.*, 16, 278
- Arendas P., Furtenbacher T., Császár A. G., 2020, *Sci. Rep.*, 10, 19489
- Arendas P., Furtenbacher T., Császár A. G., 2024, *Sci. Rep.*, 14, 794
- Azzam A. A. A., Azzam S. A. A., Aburumman K. A. A., Tennyson J., Yurchenko S. N., Császár A. G., Furtenbacher T., 2024, *J. Mol. Spectrosc.*, 405, 111947
- Azzam A. A. A., et al., 2025a, *Sci. Data*, 12, 532
- Azzam A. A. A., Tennyson J., Yurchenko S. N., Furtenbacher T., Császár A. G., 2025b, *J. Comput. Chem.*, 46, e27541
- Azzam A. A. A., AlAlawin J. M. A., Tennyson J., Yurchenko S. N., Furtenbacher T., Császár A. G., 2025c, *J. Quant. Spectrosc. Radiat. Transf.*, 343, 109485
- Balashov A. A., Raj A., Wójciewicz S., Ciurylo R., Lisak D., Bielska K., 2024, *J. Quant. Spectrosc. Radiat. Transf.*, 320, 108978
- Barnfield M., Polyansky O. L., Yurchenko S. N., Tennyson J., 2026, *J. Mol. Spectrosc.*
- Biassoni F., Borsa F., Haardt F., Rainer M., 2024, *A&A*, 691, A283
- Bunker P. R., Jensen P., 1998, *Molecular Symmetry and Spectroscopy*, 2 edn. NRC Research Press, Ottawa
- Butz A., et al., 2011, *Geophys. Res. Lett.*, 38, L14812
- Carleo I., et al., 2022, *A&A*, 164, 101
- Chubb K. L., et al., 2021, *A&A*, 646, A21
- Chubb K. L., et al., 2024, *RASTI*, 3, 636
- Crisp D., et al., 2004, *Adv. Space Res.*, 34, 700
- Devi V. M., Benner D., H. Smith M. A., Rinsland C. P., 1998, *J. Quant. Spectrosc. Radiat. Transf.*, 60, 771
- Fedorova A., Bézard B., Bertaux J.-L., Korabiev O., Wilson C., 2015, *Planet Space Sci.*, 113–114, 66
- Frediani J., et al., 2025, *A&A*, 701, A14
- Freedman R. S., Lustig-Yaeger J., Fortney J. J., Lupu R. E., Marley M. S., Lodders K., 2014, *The Astrophysical Journal Supplement Series*, 214, 25
- Furtenbacher T., Császár A. G., Tennyson J., 2007, *J. Mol. Spectrosc.*, 245, 115
- Gal Y., Ghahramani Z., 2016, in Balcan M. F., Weinberger K. Q., eds, *Proceedings of Machine Learning Research Vol. 48, Proceedings of The 33rd International Conference on Machine Learning*. PMLR, New York, New York, USA, pp 1050–1059
- Gamache R. R., Lamouroux J., 2013, *J. Quant. Spectrosc. Radiat. Transf.*, 130, 158
- Gamache R. R., Lamouroux J., Blot-Lafon V., Lopes E., 2014, *J. Quant. Spectrosc. Radiat. Transf.*, 135, 30
- Gamache R. R., Vispoel B., Tennyson J., Yurchenko S. N., Polyansky O. L., Gordon I. E., Hargreaves R. J., Huang X., 2025, *J. Quant. Spectrosc. Radiat. Transf.*, 345, 109568
- Glidden A., Seager S., Petkowski J. J., Ono S., 2023, *Life*, 13, 2325
- Gordon I. E., et al., 2022, *J. Quant. Spectrosc. Radiat. Transf.*, 277, 107949
- Hargreaves R. J., Gordon I. E., Rey M., Nikitin A. V., Tyuterev V. G., Kochanov R. V., Rothman L. S., 2020, *ApJS*, 247, 55
- Hargreaves R. J., Gordon I. E., Huang X., Toon G. C., Rothman L. S., 2024, *J. Quant. Spectrosc. Radiat. Transf.*, p. 109324
- Hashemi R., et al., 2020, *J. Quant. Spectrosc. Radiat. Transf.*, 256, 107283
- Heng K., Lyons J. R., 2016, *ApJ*, 817, 149
- Holmberg M., Madhusudhan N., 2024, *A&A*, 683, L2
- Huang X., Schwenke D. W., Tashkun S. A., Lee T. J., 2012, *J. Chem. Phys.*, 136, 124311
- Huang X., Freedman R. S., Tashkun S. A., Schwenke D. W., Lee T. J., 2013, *J. Quant. Spectrosc. Radiat. Transf.*, 130, 134
- Huang X., Gamache R. R., Freedman R. S., Schwenke D. W., Lee T. J., 2014, *J. Quant. Spectrosc. Radiat. Transf.*, 147, 134
- Huang X., Schwenke D. W., Freedman R. S., Lee T. J., 2017, *J. Quant. Spectrosc. Radiat. Transf.*, 203, 224
- Huang X., Schwenke D. W., Freedman R. S., Lee T. J., 2022, *J. Phys. Chem. A*
- Huang X., Freedman R. S., Tashkun S., Schwenke D. W., Lee T. J., 2023, *J. Mol. Spectrosc.*, 392, 111748
- Ibrahim M. T. I., Alatoom D., Furtenbacher T., Császár A. G., Yurchenko S. N., Azzam A. A. A., Tennyson J., 2024, *J. Comput. Chem.*, 45, 969

- Irwin P. G. J., et al., 2008, *J. Quant. Spectrosc. Radiat. Transf.*, 109, 1136
- Jiménez-Monferrer S., et al., 2021, *Icarus*, 353, 113830
- Karlovetz E. V., et al., 2021, *J. Quant. Spectrosc. Radiat. Transf.*, 276, 107896
- Kochanov R., Perevalov V., 2025, *J. Quant. Spectrosc. Radiat. Transf.*, 341, 109428
- Line M. R., et al., 2017, *AJ*, 848, 83
- Madhusudhan N., Sarkar S., Constantinou S., Holmberg M., Piette A. A. A., Moses J. I., 2023, *ApJL*, 956, L13
- Mansour M. H. I., Azzam A. A. A., Tennyson J., Yurchenko S. N., Furtenbacher T., Császár A. G., 2025, *Mol. Phys.*, p. e2550568
- Mant B. P., Yachmenev A., Tennyson J., Yurchenko S. N., 2018, *MNRAS*, 478, 3220
- Mayo A. W., Fortenbach C. D., Louie D. R., Dressing C. D., Turtelboom E. V., Giacalone S., Harada C. K., 2025, Detection of H<sub>2</sub>O and CO<sub>2</sub> in the Atmosphere of the Hot Super-Neptune WASP-166b with JWST ([arXiv:2501.00609](https://arxiv.org/abs/2501.00609)), <https://arxiv.org/abs/2501.00609>
- McKemmish L. K., Bowesman C. A., Kefala K., Perri A. N., Syme A. M., Yurchenko S. N., Tennyson J., 2024, *RASTI*, 3, 565
- Medvedev E. S., Ushakov V. G., 2022, *J. Quant. Spectrosc. Radiat. Transf.*, 288, 108255
- Medvedev E. S., Meshkov V. V., Stolyarov A. V., Ushakov V. G., Gordon I. E., 2016, *J. Mol. Spectrosc.*, 330, 36
- Medvedev E. S., Ushakov V. G., Conway E. K., Upadhyay A., Gordon I. E., Tennyson J., 2020, *J. Quant. Spectrosc. Radiat. Transf.*, 252, 107084
- Min M., Ormel C. W., Chubb K., Helling C., Kawashima Y., 2020, *A&A*, 642, A28
- Mollière P., Wardenier J. P., van Boekel R., Henning T., Molaverdikhani K., Snellen I. A. G., 2019, *A&A*, 627, A67
- Mondelain D., Campargue A., Gamache R. R., Hartmann J.-M., Gibert F., Wagner G., Birk M., Röske C., 2025, *J. Quant. Spectrosc. Radiat. Transf.*, 333, 109271
- Obaidata S. A. M., Azzam A. A. A., Tennyson J., Yurchenko S. N., Furtenbacher T., Császár A. G., 2025, *J. Mol. Spectrosc.*, 340, 109444
- Oppenheimer B. R., et al., 2013, *AJ*, 768, 24
- Oyafuso F., et al., 2017, *J. Quant. Spectrosc. Radiat. Transf.*, 203, 213
- Paszke A., et al., 2019, Advances in neural information processing systems, 32
- Pollack J. B., et al., 1993, *Icarus*, 103, 1
- Polyansky O. L., Bielska K., Ghysels M., Lodi L., Zobov N. F., Hodges J. T., Tennyson J., 2015, *Phys. Rev. Lett.*, 114, 243001
- Refaat T. F., Singh U. N., 2024, in IGARSS 2024 - 2024 IEEE International Geoscience and Remote Sensing Symposium. pp 930–933, [doi:10.1109/IGARSS53475.2024.10642559](https://doi.org/10.1109/IGARSS53475.2024.10642559)
- Roche S., et al., 2021, *AMT*, 14, 3087
- Rothman L. S., Young L. D. G., 1981, *J. Quant. Spectrosc. Radiat. Transf.*, 25, 505
- Rothman L. S., et al., 2010, *J. Quant. Spectrosc. Radiat. Transf.*, 111, 2139
- Snels M., Stefani S., Grassi D., Piccioni G., Adriani A., 2014, *Planet Space Sci.*, 103, 347
- Sokolov A., Yurchenko S. N., Tennyson J., Gamache R. R., Vispoel B., 2025, *J. Quant. Spectrosc. Radiat. Transf.*, 330, 109225
- Swain M. R., Vasisht G., Tinetti G., Bouwman J., Chen P., Yung Y., Deming D., Deroo P., 2009a, *ApJL*, 690, L114
- Swain M. R., et al., 2009b, *ApJ*, 704, 1616
- Tan Y., Kochanov V. R., Rothman L. S., Gordon I. E., 2019, *J. Quant. Spectrosc. Radiat. Transf.*, 124, 11580
- Tan Y., Skinner F. M., Samuels S., Hargreaves R. J., Hashemi R., Gordon I. E., 2022, *ApJS*, 262, 40
- Tashkun S. A., Perevalov V. I., 2011, *J. Quant. Spectrosc. Radiat. Transf.*, 112, 1403
- Tashkun S., Perevalov V., Teffo J.-L., Bykov A., Lavrentieva N., 2003, *J. Quant. Spectrosc. Radiat. Transf.*, 82, 165
- Tashkun S. A., Perevalov V. I., Gamache R. R., Lamouroux J., 2015, *J. Quant. Spectrosc. Radiat. Transf.*, 152, 45
- Tennyson J., Hill C., Yurchenko S. N., 2013, in 6<sup>th</sup> international conference on atomic and molecular data and their applications ICAMDATA-2012. AIP, New York, pp 186–195, [doi:10.1063/1.4815853](https://doi.org/10.1063/1.4815853)
- Tennyson J., Furtenbacher T., Yurchenko S. N., Császár A. G., 2024a, *J. Quant. Spectrosc. Radiat. Transf.*, 316, 108902
- Tennyson J., et al., 2024b, *J. Quant. Spectrosc. Radiat. Transf.*, 326, 109083
- Tobias R., et al., 2020, *Nature Comm.*, 11, 1708
- Toth R. A., Brown L. R., Miller C. E., Devi V. M., Benner D. C., 2008, *J. Quant. Spectrosc. Radiat. Transf.*, 109, 906
- Vispoel B., Gamache R. R., 2024, *J. Quant. Spectrosc. Radiat. Transf.*, 316, 108896
- Wang R., Balciunaite U., Chen J., Yuan C., Owens A., Tennyson J., 2023, *J. Quant. Spectrosc. Radiat. Transf.*, 306, 108617
- Wattson R. B., Rothman L. S., 1986, *J. Mol. Spectrosc.*, 119, 83
- Webster C. R., et al., 2013, *Science*, 341, 260
- Yurchenko S. N., Mellor T. M., 2020, *J. Chem. Phys.*, 153, 154106
- Yurchenko S. N., Thiel W., Jensen P., 2007, *J. Mol. Spectrosc.*, 245, 126
- Yurchenko S. N., Barber R. J., Yachmenev A., Thiel W., Jensen P., Tennyson J., 2009, *J. Phys. Chem. A*, 113, 11845
- Yurchenko S. N., Barber R. J., Tennyson J., Thiel W., Jensen P., 2011, *J. Mol. Spectrosc.*, 268, 123
- Yurchenko S. N., Yachmenev A., Ovsyannikov R. I., 2017, *J. Chem. Theory Comput.*, 13, 4368
- Yurchenko S. N., Mellor T. M., Freedman R. S., Tennyson J., 2020, *MNRAS*, 496, 5282
- Yurchenko S. N., Mellor T., Tennyson J., 2024, *MNRAS*, 534, 1364
- Zak E., Tennyson J., Polyansky O. L., Lodi L., Tashkun S. A., Perevalov V. I., 2016, *J. Quant. Spectrosc. Radiat. Transf.*, 177, 31
- Zak E. J., Tennyson J., Polyansky O. L., Lodi L., Zobov N. F., Tashkun S. A., Perevalov V. I., 2017a, *J. Quant. Spectrosc. Radiat. Transf.*, 189, 267
- Zak E. J., Tennyson J., Polyansky O. L., Lodi L., Zobov N. F., Tashkun S. A., Perevalov V. I., 2017b, *J. Quant. Spectrosc. Radiat. Transf.*, 203, 265

This paper has been typeset from a  $\text{\LaTeX}$  file prepared by the author.